Solar Energy 173 (2018) 1315–1322

Contents lists available at ScienceDirect

Solar Energy

journal homepage: www.elsevier.com/locate/solener

Strain and layer modulated electronic and optical properties of low dimensional perovskite methylammonium lead iodide: Implications to solar cells

Narayan N. Som[a], P.M.W.P. Sampath[b], Shweta D. Dabhi[c], Venu Mankad[d], Satyam Shinde[e], M.L.C. Attygalle[b], Prafulla K. Jha[a,*]

[a] Department. of Physics, Faculty of Science, The M.S. University of Baroda, Vadodara 390002, India
[b] Department of Physics, University of Sri Jayewardenepura, Nugegoda, Sri Lanka
[c] P. D. Patel Institute of Applied Science, Charotar University of Science and Technology, CHARUSAT-Campus, Changa 388 421, India
[d] Department of Physics, School of Technology, GITAM University, Hyderabad Campus, Hyderabad 502329, India
[e] School of Technology, Pandit Deendayal Petroleum University, Gandhinagar, Gujarat 382007, India

ARTICLE INFO

Keywords:
Low dimensional perovskite
Density functional theory
Electronic properties
Solar cell parameters

ABSTRACT

In the present work we report the effect of quantum confinement, biaxial and uniaxial strains on electronic properties of two dimensional (2D), one dimensional (1D) and layered system of Methylammonium lead iodide (MAPI) in cubic phase using first principles calculations based on density functional theory for its implications to solar cell. Our studies show that the bandgap of MAPI is dimension dependent and is maximum for 1D. We also found that the band gap of 2D MAPI can be modulated through application of biaxial strain, which shows linear relation with strain; compressive strain decreases the band gap whereas tensile strain increases the band gap. 1D MAPI shows near parabolic response towards strain which increases with compressive and tensile strain. Our studies show that the 2D MAPI is better for a solar cell due to lower effective mass of electron and hole arising from the strong s-p anti-bonding coupling. The calculated solar cell parameters suggest that the 2D MAPI is best suited for solar cell applications. The calculated open circuit voltage, fill factor and efficiency are highest for 2D MAPI. The highest theoretical efficiency of 2D MAPI is 23.6% with mesoporous (mp)-TiO_2 electrode.

1. Introduction

Perovskite crystals with chemical formula ABO_3 are known for their complex landscape and useful physical properties such as magnetic, ferroelectric and two dimensional electronic conductivity (Cohen, 1992; Peña and Fierro, 2001). Last few years have witnessed a tremendous effort for the organic – inorganic perovskites not only due to their more complicated structure than that of organic perovskites arising due to many possible orientation of organic materials (Baikie et al., 2013) but also due to phenomenal advancement in the solid state solar cells (Burschka et al., 2013; Jeon et al., 2014; Jung and Park, 2015; Kim et al., 2012; Lee et al., 2012; Stoumpos et al., 2013; Zhou et al., 2014). The photovoltaic efficiency in the solid state solar cells has reached its maximum about 21% (Jung and Park, 2015; "Natl. Renew. Energy Lab" https://www.nrel.gov/pv/assets/images/efficiency-chart.png.; Zhou et al., 2014). Further, it is observed that the organic cations and substitution of metal halides affect the bandgap through alternation of inorganic framework (Eperon et al., 2014; Filip et al., 2014; Noh et al., 2013). The organic-inorganic halide perovskites have unit cell generally composed of AMX_3 (where A = $CH_3NH_3^+$, or $(H_2N)_2CH^+$, Cs^+; M = Sn^{2+}, Pb^{2+} and X = Cl^-, Br^-, I^-) (Mitzi, 2004, 2001). The best example of this alternation is Cs which is largest atom in the group I to hold cubic perovskite structure but the molecule CH_3NH_3 is larger than Cs, which makes $CH_3NH_3PbI_3$ (MAPI where MA represents CH_3NH_3 cation) more stable and perform better than $CsPbI_3$ (Zhang et al., 2015). Furthermore, they are known for many interesting properties such as high optical absorption spectra range, a long carrier diffusion and most importantly tuneable bandgap (Dong et al., 2015; Stranks et al., 2013) which leads them to be useful in various applications of optoelectronics and photonic devices including solar cells, photodetectors, light emitting diodes, field effect-transistors (FET), waveguides and nano lasers (Chin et al., 2015; Kojima et al., 2009; Snaith, 2013; Tan et al., 2014; Wang et al., 2015, 2016; Zhu et al., 2015). MAPI which was first reported by Weber (Weber, 1978) in the cubic crystal structure consequently has been studied intensively as a solid state solar cell due to its high photovoltaic efficiency over 20%

* Corresponding author.
E-mail address: pk.jha-phy@msubaroda.ac.in (P.K. Jha).

https://doi.org/10.1016/j.solener.2018.06.052
Received 1 May 2018; Received in revised form 2 June 2018; Accepted 12 June 2018
Available online 30 October 2018
0038-092X/

(Burschka et al., 2013; Green et al., 2014; Heo et al., 2013; Liu et al., 2013).

Earlier works show that the orientationally disordered nature of organic-inorganic halide perovskites with high effective lattice symmetry on average is origin of their high performance (Frost and Walsh, 2016). To maintain high symmetry cubic structure, the ionic radii of A, M and X in perovskite AMX_3 should satisfy tolerance factor t (where $t = (R_A + R_X)/\{\sqrt{2}\ (R_M + R_X)\}$; R_A, R_M and R_X is atomic radii of MA, Pb and I respectively) close to 1. The cubic structure may exists when t lies between 0.89 and 1 at finite temperature, smaller t leads to lower symmetry such as tetragonal or orthorhombic and $t > 1$ destabilizes bulk network of cubic phase leading to a two dimensional layered structure (Yin et al., 2015). One of the major challenges of bulk MAPI in the development of solar cells is its poor stability towards moisture and oxygen in the environment (Zhang et al., 2015). MAPI has AMX_3 three dimensional lattice framework. The slow radiative recombination (Zhu et al., 2015) arising from the low exciton binding energy together with the poor stability of these MAPI materials can produce unstable operation and fast degradation in light emitting devices (Yang et al., 2015). However, the lower dimensional MAPI characterized by inorganic layers spaced using organic ligands (Mitzi et al., 1994) provided an excellent combination of structural and photophysical properties, such as dimension dependent bandgap (Ishihara et al., 1989), increased exciton binding energy and better stability compared to bulk MAPI (Yang et al., 2015). Recently, a two dimensional (2D) hybrid solar cell device consisting of a layered perovskite absorber has been fabricated under ambient conditions (Cao et al., 2015; Liu et al., 2016; Zhou et al., 2016), which has better moisture stability compared to the bulk phase (Cao et al., 2015). The electronic structure study using density functional theory (DFT) including relative spin-orbit coupling effect shows an increase in energy bandgap (E_g) of MAPI due to the confinement effect in 2D structure (Kamminga et al., 2016). In addition, several types of hetero-structures have been developed combining MAPI and carbon materials such as graphene, fullerenes and carbon nanotubes (CNT) for enhancing stability, reducing drifts and hysteric effects to be used in semi-transparent flexible and high sensitive photo resister solar cells (He et al., 2015; Jeng et al., 2013; Lee et al., 2015; Li et al., 2014; Shao et al., 2014; Spina et al., 2015; You et al., 2015). The one dimensional (1D) MAPI in nanowire forms has been successfully used in a field effect phototransistor fabrications (Spina et al., 2016). The sensitization of individual CNT-FETs with a network of MAPI nanowires resulted quite good light responsivities and external quantum efficiency.

The performance of a solar cell depends very much on open circuit voltage (V_{oc}) which is quite high in the case of perovskite based solar cells (Yin et al., 2015). The ratio V_{oc}/E_g of MAPI indicates its suitability to be used as a solar cell absorber which is comparable with some of the best solar cell absorbers (Yin et al., 2015). Yin et al calculated the solar cell parameters such as V_{oc}, short circuit current (J_{sc}) and Fill Factor (FF) as a function of absorber thickness for MAPI and found matching quite well with available experimental values except FF (Yin et al., 2015). Further, previous studies show that the V_{oc} and FF of any device highly depends on the high level of perovskite absorbers, conduction band (CB) of mesoporous (mp) electrode such as TiO_2 and transporting hole materials (Ryu et al., 2014).

Besides confinement, strain which is unavoidable due to mismatch between substrate and grown structure plays a vital role in fabrication of a device including solar cells. Previous studies have shown that the strain is a powerful strategy to tune electronic properties of low dimensional systems (Dabhi and Jha, 2015; Logan and Peng, 2009; Pillai et al., 2016). Another aspect which can be useful to tune the electronic and optical properties for new electronic and optical devices is tuning number of layers in a 2D materials (Bernardi et al., 2017; Song et al., 2016). The strain is defined as $\epsilon = \frac{(a_0 - a)}{a_0}$, where a_0 and a are the lattice constants for unstrained and strained structures respectively.

Motivated with above facts we have investigated the electronic properties, optical properties and solar cell parameters of bulk, 2D and 1D MAPI using first principles calculation based on density functional theory to understand the role of dimensionality on these parameters. Further, we explored the electronic of 2D MAPI by varying the number of layers i.e. by changing layer thickness and applying strain. Our particular interest in the study of strain dependent electronic properties is to find out the location of conduction/valence band edges and understand the mechanism in bulk, 2D and 1D structures. Finally we have calculated the open circuit voltage (V_{oc}), filter factor (FF), short circuit current density (J_{sc}) and efficiency (η) using Shockley and Quessier (SQ) model.

2. Computational details

The calculations in the present study were performed using state-of-art first principles calculation based on density functional theory (DFT) within the plane wave pseudopotentials as implemented in Quantum Espresso code (Giannozzi et al., 2009). The exchange correlation interaction was treated within the generalized gradient approximation (GGA) given by Perdew, Burke and Ernzerhof (PBE) (Perdew and Burke, 1996). An energy cutoff of 150 Ry is used for electronic wave function for bulk, two-dimensional and one-dimensional MAPI. A grid of $7 \times 7 \times 7$ for bulk, $7 \times 7 \times 1$ for two-dimensional and $7 \times 1 \times 1$ for one dimensional MAPI was sampled in reciprocal space. Brillouin zone (BZ) integration was performed using Monkhorst-Pack convergence analysis. The energy convergence value between two consecutive steps was chosen as 10^{-4} eV and maximum Hellmann-Feynman force acting on each atom was less than the 0.001 eV/Å to achieve a good convergence. After successful prediction of bandgap in MAPI with different order of confinement, layer and strain, we calculated optical properties of Bulk, 2D and 1D MAPI with random phase approximation (RPA) using the long wavelength expression for imaginary part of dielectric tensor (Bercx et al., 2017; Gajdoš et al., 2006; Harl et al., 2007). The real part of the dielectric tensor is determined using the Kramers-Kronig relation. After acquiring the dielectric function, we have calculated the absorption coefficient $\alpha = \frac{4\pi E}{hc}\hat{k}(E)$ with h and c as Planck's constant and speed of light respectively. Here $\hat{k}(E) = \sqrt{\sqrt{(\varepsilon_r(\omega)^2 + \varepsilon_i(\omega)^2)} - \varepsilon_r(\omega)}$.

3. Results and discussion

Before starting the calculation of the different properties of MAPI in various circumstances such as under confinement, with different number of layers and strain, we developed the optimized structure of bulk, two-dimensional (2D) and one dimensional (1D) MAPI which are presented in Fig. 1(a–c). The 2D structurewas modeled by introducing a vacuum of 20 Å between two MAPI layers in Z direction whereas we introduced vacuum of 20 Å along Y and Z directions for modelling the 1D structure. Table 1 summarizes the optimized lattice constants and energy bandgap for all considered structures. There is a good agreement between the present and available experimental (Baikie et al., 2013; Egger and Kronik, 2014; Quarti et al., 2015; Stoumpos et al., 2013) and theoretical (Egger and Kronik, 2014; Quarti et al., 2015; Yin et al., 2015) data. It is noteworthy that the present electronic band structure calculations are carried out without consideration of spin orbit coupling (SOC) as it is found that the SOC underestimates band gap in this case (Quarti et al., 2015). In addition, it is also found that the inclusion of SOC in Pb-based compounds does not alters their structural proerties (Whalley et al., 2017). We found that the presnet GGA calculations give better results as compared to scalar-relativitic SR(SOC)-DFT, SOC-GW and even matches with SR-DFT calculations for bulk MAPI (Quarti et al., 2015). The better results in our case than other more complicated methods can be attributed to the cancellation of errors. Fig. 2(a–c) present the electronic band structure of bulk, 2D and 1D MAPI, which

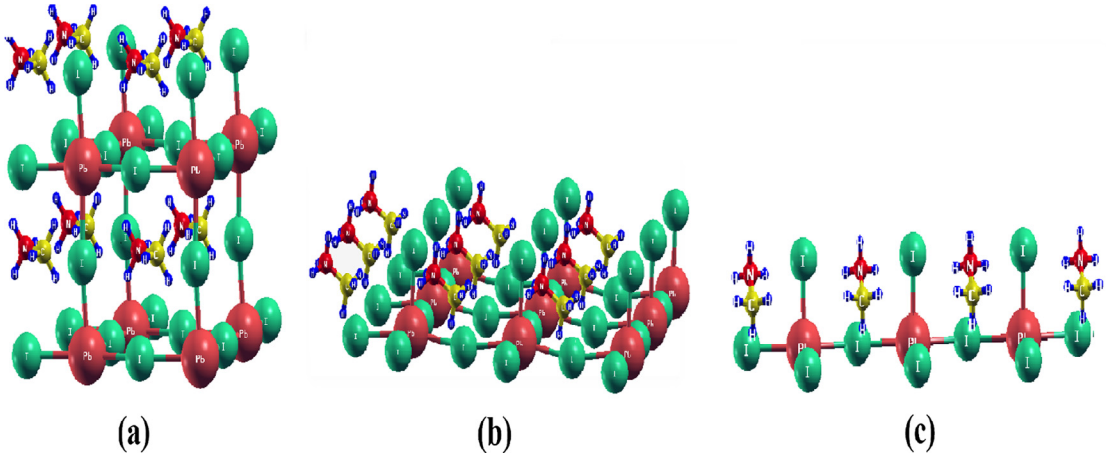

Fig. 1. Atomic model for the cubic phase of MAPI. (a) bulk, (b) two-dimensional and (c) one-dimensional.

Table 1
Calculated lattice constant (Å) and band gap for bulk, two dimensional and one dimensional Methylammonium lead iodide (MAPI) in cubic phase along with other available data.

Lattice parameter (Å)	Bandgap (eV)	Electron effective mass(m_e)	Hole effective mass(m_e)
Bulk			
6.46	1.675	0.29	0.31
a = 6.28[a], 6.31[b], 6.33[c], 6.39[d] 6.38[h],a = b = 6.49c = 6.50[h**]	1.53[d], 1.14[d], 1.28[e$],1.69[e#] 1.62[e$$], 0.59[e##],1.52[f]	0.35[g] 0.18[g(soc)]	0.31[g] 0.21[g(soc)]
2D			
a = b = 6.383, c = 20	2.242, 2.24[f*]	0.24	0.29
1D			
a = 6.38, b = c = 20	2.42	0.21	0.27

[a] Ref. Stoumpos et al. (2013) exp.
[b] Ref. Baikie et al. (2013) exp.
[c] Ref. Quarti et al. (2015) exp.
[d] Ref. Frost and Walsh (2016) PBE.
[e] Ref. Quarti et al. (2015) exp. [#](300 K), SOC-GW[$], Scalar relativistic(SR)-DFT[$$], SOC[##].
[f] Ref. Cao et al. (2015) exp.,[*]Bandgap of $(CH_3(CH_2)_3NH_3)_2PbI_4$
[g] Ref. (Yin et al. (2014b).
[h] Ref. Egger and Kronik (2014) PBE,[**]lattice parameter for pseudo cubic

clearly show an increase in the bandgap as increasing the degree of confinement i.e. going from bulk to 2D to 1D structure. Table 1 together with Fig. 2 clearly depict that the confinement significantly affects the bandgap. It is clearly seen from the band structures that the nature of band gap in MAPI does not change with the order of confinement. The direct bandgap of 1.675 eV at **R**-point, 2.24 eV at **M**-point and 2.42 eV at **X**-point of the BZ is observed for bulk, 2D and 1D respectively. Detailed analysis of the band structure for bulk depicts that the valence band mainly consists 5s and 5p orbitals of I and 6d and 6s orbitals of Pb. The upper most valence band has strong antibonding coupling between I p and Pb s orbitals with negligible contribution of Pb d orbital and are predominantly found between −3 eV and 0 eV. The MA cation does not show any contribution around the band edge, which has the range from −7 eV to −9 eV. The lowest conduction band is mainly contributed by Pb p and I s orbitals. In case of 2D MAPI, due to confinement in z-direction there is a strong antibonding coupling between s orbital of Pb atom and p orbital of adjacent I atom. The contribution of Pb p orbital is more in the case of 2D MAPI as compared to its bulk counterpart.

To understand the effect of degree of confinement on bandgap of bulk, 2D and 1D MAPI, we have plotted the partial density of states (PDOS) in Fig. 3. We found that the methylammonium ion $(CH_3NH_3)^+$ *i.e* MA) does not play any direct role in alteration of electronic properties. It shows weak dependence on the orientation of MA ion in inorganic framework due to weak Van der Waals interaction (Yin et al., 2014a). It is seen from the PDOS that the conduction band minimum (CBM) is influenced by p orbital of the Pb atom, whereas the valence band maximum (VBM) is influenced by s and p orbitals of I atom. The ratio of DOS at valence band edge and conduction band edge is highest in 1D MAPI, which indicates greater relaxation rates for holes than

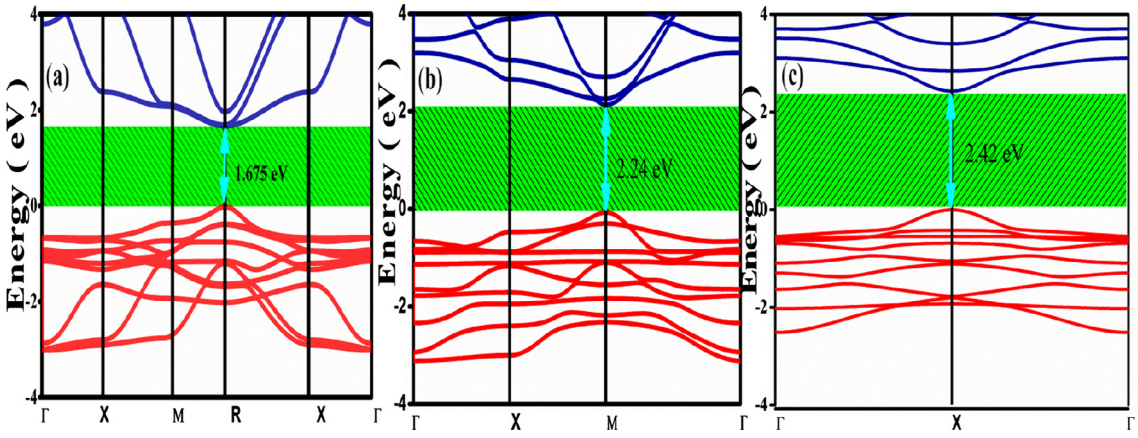

Fig. 2. Electronic band structure of cubic MAPI : (a) bulk, (b) two-dimensional and (c) one-dimensional MAPI.

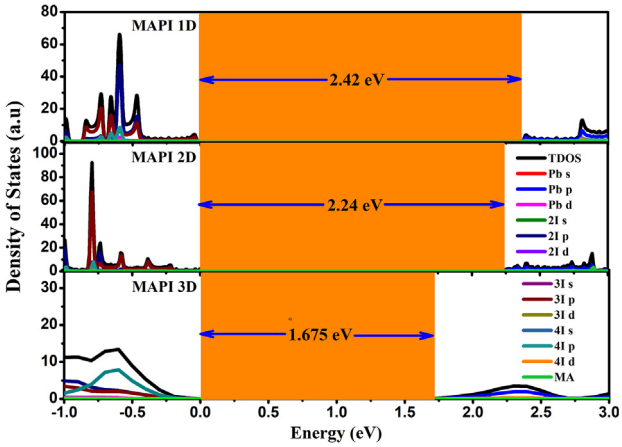

Fig. 3. Partial electronic density of states (PDOS) for bulk, two-dimensional and one-dimensional MAPI.

electrons. Further, the high DOS near valence band generate and transfer more electrons and are responsible to enhance optical properties of MAPI. The performance of a solar cell depends on its band gap, optical absorption and electric transport efficiency of carriers that depends on their effective mass. Keeping this in view, we have calculated the effective mass of electron and hole by a parabolic fitting to the band edge along **R-X**, **M-Γ** and **X-Γ** directions for bulk, 2D MAPI and 1D MAPI respectively. The effective mass of electron and hole is calculated using equation $m^* = \hbar^2\left[\frac{\partial^2 \in (k)}{\partial K^2}\right]^{-1}$. The effective mass of electron and hole in 2D and 1D MAPI is lower compared to its bulk counter-part due to the flat bands near band edge. Moreover, balanced effective mass for all cases shows ambipolar condition. The lower effective mass of electron and hole, which arise from the strong s-p anti-bonding coupling, is quite useful for a p-i-n configuration. This suggests that the 2D MAPI is better for p-i-n configurations of thin-film solar cells. However, this is not true for 1D MAPI where confinement occurs in two directions. The upper most bands of valence band region is contributed by I s orbital with negligible contribution of Pb d and Pb s orbitals. The s-p antibonding coupling is weaker compared to both bulk and 2D MAPI leading to a large bandgap. This suggest a different use of 1D MAPI particularly in light emitting diode (LED), field-effect transistor etc. (Spina et al., 2016).

4. Implications to solar cell

For a material to be used in solar cell applications, we have to calculate solar cell performance parameters such as open circuit voltage, short circuit current density, fill factor and efficiency (Bercx et al., 2017; Ryu et al., 2014; Yin et al., 2015). The optimization of optical and dielectric properties of perovskite solar cell is a crucial issue (Ryu et al., 2014; Yin et al., 2015; Zhou et al., 2016). Fig. 4(a & b) present the calculated real and imaginary parts of the dielectric constant $\varepsilon_r(\omega)$ and $\varepsilon_i(\omega)$ respectively for bulk, 2D and 1D MAPI.

The absorption coefficient plays a vital role in the fabrication of solar cells. The photon with smaller energy than the band gap of material cannot be absorbed hence leading to no absorption and causes a loss of energy. The dielectric function is highest around 4.2–4.5 eV for all cases. It attains minima around 4.6–5.0 eV suggesting MAPI to be transparent for high-energy incident photon and exhibit metallic nature in this region. The absorption coefficients, which depend on joint density of state (JDOS), can be calculated using dielectric constants. Fig. 5(a) presents the absorption spectra of bulk, 2D and 1D MAPI, which clearly depicts a blue shift confirming an increase in the bandgap of 1D MAPI as compared to bulk and 2D. In the case of 1D MAPI, higher photon energy is required for the absorption of photons compared to bulk and 2D counterparts. Fig. 5(b) shows that the maximum JDOS for 1D MAPI indicating lesser absorption efficiency compared to bulk and 2D MAPI. From JDOS, it is clear that the absorption efficiency is highest for 2D MAPI and hence it is most suitable for the solar cell.

Above results clearly show promising electronic and optical properties for 2D MAPI. To ensure that the 2D MAPI is best suitable for solar cell, we have calculated the V_{oc}, FF, J_{sc} and η and presented them in Table 2. The *Voc* is calculated using expression $Voc = E_{LUMO}^{MAPI} - E_{CB}^{Tio_2}$ (for mesoporous (mp)-TiO_2 electrode) and $Voc = |E_{HOMO}^{MAPI}| - |E_{LUMO}^{PCBM}| - 0.3$ (for phenyl C_{61} or C_{70} butyric acid methyl ester (PCBM) electrode) (El alamy et al., 2017), where $E_{CB}^{Tio_2}$ and E_{LUMO}^{PCBM} are conduction band minima of TiO_2 and LUMO level of PCBM. The TiO_2 and PCMB are used as mesoporous (mp)-TiO_2 electrode and phenyl C_{61} or C_{70} butyric acid methyl ester (PCBM) electrode (Bourass et al., 2013; El alamy et al., 2017; Ryu et al., 2014). The schematic of the solar cell fabrication is presented in Fig. S1. In our calculation, we consider the $E_{CB}^{Tio_2} = 4.0\ eV$ and $E_{CB}^{Tio_2} = 3.2\ eV$ (Bourass et al., 2013; El alamy et al., 2017). Table 2 depicts that the maximum V_{oc} is found as 1.75 eV, 2.15 eV and 1.14 eV for 1D, 2D and bulk MAPI respectively in case of TiO_2. The calculated V_{oc} is then used to calculate the fill factor using expression $FF = \frac{\vartheta_{oc} - \ln(\vartheta_{oc} + 0.72)}{\vartheta_{oc} + 1}$; $\vartheta_{oc} = \frac{q \times V_{oc}}{K_B T}$ (Green et al., 2014; Leilaeioun and Holman, 2016). The theoretical J_{sc} (short circuit current density) can be calculated using equation $J_{sc} = \int_0^\infty eA(E)I_{sun}(E)dE$; I_{sun} is the photon flux density from AM1.5G spectrum and A (E) is absorbance. The attainable current density for a particular bandgap can be obtained by integrating the spectral distribution.

Photovoltaic cell efficiency is universally accepted due to Shockley and Quessier (SQ) that depends on band gap (E_g) of material gives $A(E) = 1$ for $E \geq E_g$ and $A(E) = 0$ for $E < E_g$, while under spectroscopic limited maximum efficiency (SLME) absorbance is thickness dependent given as $A(E) = 1 - e^{2\alpha L}$; α is absorption coefficient and L is thickness of material (Yu and Zunger, 2012). We use SQ in our calculation for J_{sc}. The calculated efficiency of solar cell of bulk, 2D and 1D MAPI obtained using $\eta = \frac{FF.J_{sc}.V_{oc}}{P_{in}}$; P_{in} is the AM1.5 solar irradiation of 100 mW cm^{-2} is presented in Table 2. Our results on solar cell parameters agree well with earlier reported experimental (Gelmetti et al., 2017; Liu et al., 2013; Ryu et al., 2014) and other theoretical (Sha et al., 2015; Yin et al., 2015) values within the constraint of thickness of absorber. Our calculated efficiency however is about 14% lower than the efficiency obtained by Sha et al. (2015) which can be attributed to the use of light trapping and angular restriction structure using reflecting surface and lower absorber thickness. The efficiency is highest for 2D MAPI followed by bulk and 1D MAPI in case of TiO_2. These suggest that the 2D MAPI is most promising candidate to be used in solar cell.

The solar performance parameters can be tuned using electronic bandgap of materials. With this motivation, we tuned the electronic properties of MAPI by applying biaxial and uniaxial strain respectively to 2D and 1D MAPI. We have imposed strain in the present calculations from −6% to 6% for both and present bandgap variation with strain in Fig. 6(a). It is clear from this figure that the bandgap of 2D MAPI increases on imposing tensile strain (positive strain) and reduces imposing on compressive strain (negative strain). However, in case of 1D MAPI, the bandgap increases in both tensile and compressive strains and shows parabolic behavior with strain. In case of 1D MAPI a direct bandgap nature is observed (Fig. S2(a)). Moreover, after applying uniaxial strain an increase in bandgap is found without altering the band nature. It is clearly seen from Fig. 6(b) that only energy of conduction band minima (CBM) at **X** (CBM-**X**) and CBM at **Γ** (CBM- **Γ**) increases with respect to strain. The parabolic nature of bandgap versus strain emerges from the parabolic nature of CBM-X. In case of 2D MAPI a progressive opening of bandgap upon increasing tensile strain is observed (Figs. S2 and Fig. 6(c)) and band nature is changed after applying compressive strain as energies of conduction band minima at **M** (CBM-**M**) and valley (CBM-**V**) crosses each other at −4% strain i.e. turns indirect in nature. Further, we analyzed the effect of number of

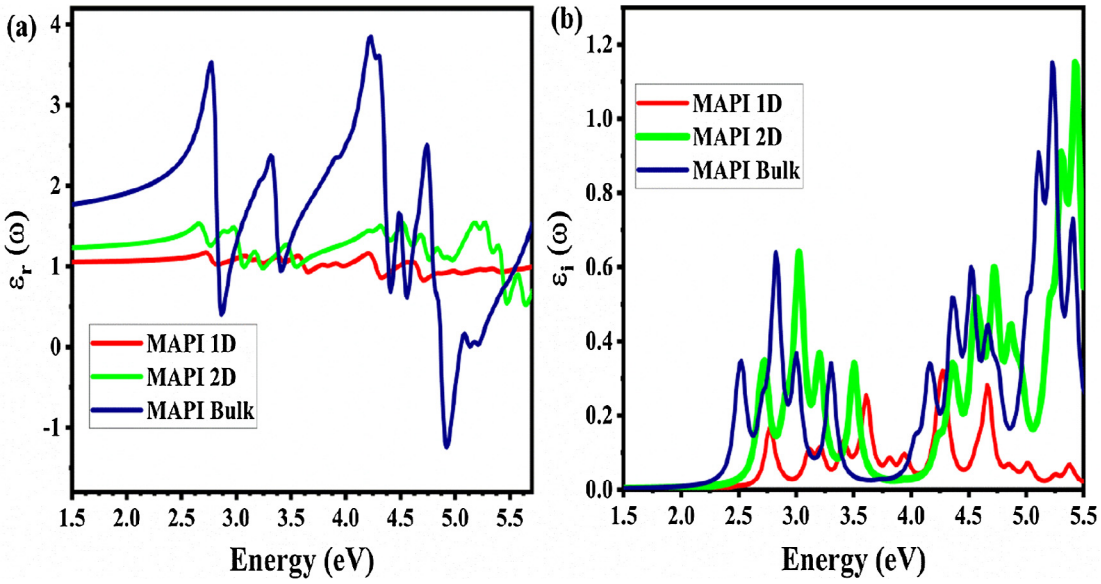

Fig. 4. (a) Calculated real part of dielectric constant and (b) imaginary part of dielectric constant of bulk, 2D and 1D MAPI.

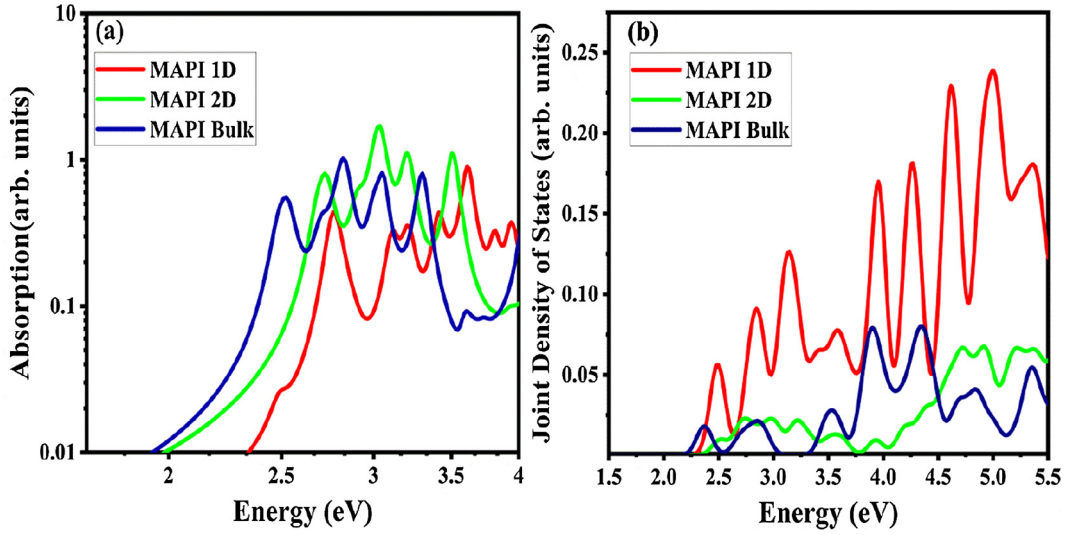

Fig. 5. (a) Absorption coefficient and (b) joint density of state (JDOS) of bulk, 2D and 1D MAPI.

Table 2
Calculated Solar cell parameters.

System	TiO_2				PCBM			
	V_{oc}(eV)	FF	J_{sc}(mA/cm^2)	η(%)	V_{oc}(eV)	FF	J_{sc}(mA/cm^2)	η(%)
Bulk	1.14	0.89	21.2	21.5	1.04	0.88	21.2	19.4
	1.04[a]	0.73[a]	21.3[a]	16.2[a]	1.07[b]	0.59[b]	12.5[b]	7.89[b]
	1.19[c]	0.89[c*]	19.2[c*]	20.33[c*]	1.35[d&]	0.91 [d&]	25.27 [d&]	30.0[d&]
	1.35[d**]	0.91[d**]	22.3[d**]	26.8[d**]	1.305 [d&&]	0.91 [d&&]	25. 97 [d&&]	30.88 [d&&]
2D	2.15	0.93	11.8	23. 6	1.74	0.91	11.8	18.7
1D	1.75	0.92	8.6	13.8	1.17	0.90	8.6	9.1

[a] Ref. Ryu et al. (2014)exp.
[b] Ref. Gelmetti et al. (2017) exp.
[c] Ref. (Yin et al. (2015) theor.
* We have calculated fill factor using Voc and efficiency.
[d] Ref. Sha et al. (2015)theor. Calculations considering flat and perfect mirror at 200 nm**, 500 nm& and 1000 nm && thickness.

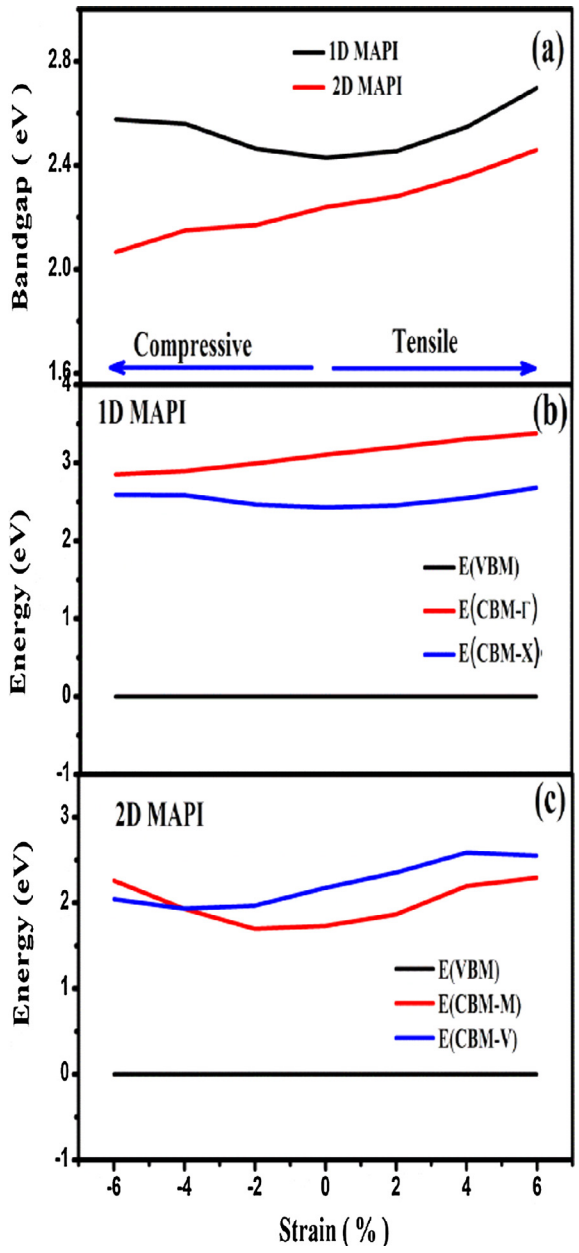

Fig. 6. (a) Change in bandgap as function of strain, (b) The calculated energies for VBM, CBM at X and CBM at Γ for MAPI 1D as function of uniaxial strain and (c) The calculated energies for VBM, CBM at M and CBM at valley for MAPI 2D as function of biaxial strain.

layers on the band structure of 2D MAPI and found that on increasing the number of layers, the direct bandgap observed at **M** point gradually decreases which is quite obvious as it approaches to bulk. This fact can be attributed to the van der Waals forces between layers, which increases with the increase of number of layers whereas this interaction is weak in case of monolayer and bilayer. Moreover, the presence of direct band gap nature is unaffected (Fig. S3) despite increasing the number of layers, that shows an advantage of multilayer 2D MAPI for optoelectronic applications. It will be easier to fabricate stable devices using few layers rather than a monolayer. However, it is disappointing that the solar cell parameters do not improve with number of layers or with the application of strain. While bandgap increases with strain, the efficiency decreases (Table S1).

5. Conclusion

In the present paper, we report electronic properties of a prospective solar cell material methylammonium lead iodide (MAPI) in bulk, 2D and 1D forms. The quantum confinement affects the band structure of MAPI. The CH_3NH_3 (MA) ion contributs less in the band structure of bulk MAPI whereas it plays a major role in tuning the bandgap of 2D and 1D MAPI. In case of 1D and 2D, DOS depicts that holes relaxation rate is much greater as compared to bulk. On applying tensile and compressive uniaxial and biaxial strains on 2D MAPI, there is a direct to indirect band transition beyond 4% of compressive strain in the case of 2D MAPI. However, no such effect is observed in 1D MAPI. The band gap of 2D MAPI decreases with the increase in the number of layers. We have also calculated the solar cell parameters such as open circuit voltage, fill factor, short circuit current density and efficiency of bulk, 2D and 1D solar cell material MAPI. Our study reports that the solar cell parameters of MAPI are highly influenced by confinement, strain and number of layers (2D case). The V_{oc}, FF, J_{sc} and η are highest in case of 2D MAPI followed by 1D and bulk. The efficiency is highest with 23. 6% in case of 2D MAPI. The solar cell parameters obtained in the present studies show trend similar to earlier studies. The present studies bring out the fact that the 2D MAPI is best-suited material for solar cell. The present studies show that the 2D and 1D will be useful for future tunable hybrid perovskite-based light emitting diode, photodetectors and solar cells.

Acknowledgement

Authors are thankful to SERB (SB/S2/CMP-0005/2013) and DST (DST/INT/SL/SLP-21/2016) for financial support. SD is thankful to DST for INSPIRE Fellowship Award. VM acknowledges the young scientist award from Science and Engineering Research Board (SR/FTP/PS-05/2014), Government of India.

Appendix A. Supplementary material

Supplementary data associated with this article can be found, in the online version, at https://doi.org/10.1016/j.solener.2018.06.052.

References

Baikie, T., Fang, Y., Kadro, J.M., Schreyer, M., Wei, F., Mhaisalkar, S.G., Graetzel, M., White, T.J., 2013. Synthesis and crystal chemistry of the hybrid perovskite (CH3NH3) PbI3 for solid-state sensitised solar cell applications. J. Mater. Chem. A 1, 5628. http://dx.doi.org/10.1039/c3ta10518k.

Bercx, M., Sarmadian, N., Saniz, R., Partoens, B., Lamoen, D., 2017. Correction: first-principles analysis of the spectroscopic limited maximum efficiency of photovoltaic absorber layers for CuAu-like chalcogenides and silicon. Phys. Chem. Chem. Phys. 19, 6292. http://dx.doi.org/10.1039/C7CP90033C.

Bernardi, M., Ataca, C., Palummo, M., Grossman, J.C., 2017. Optical and electronic properties of two-dimensional layered materials. Nanophotonics 6, 479–493. http://dx.doi.org/10.1515/nanoph-2015-0030.

Bourass, M., Fitri, A., Touimi Benjelloun, A., Benzakour, M., Mcharfi, M., Hamidi, M., Serein-Spirau, F., Jarrosson, T., Lère-Porte, J.P., Sotiropoulos, J.M., Bouachrine, M., 2013. DFT and TDDFT investigations of new thienopyrazine-based dyes for solar cells: effects of electron donor groups. Der Pharma Chem. 5, 144–153.

Burschka, J., Pellet, N., Moon, S.J., Humphry-Baker, R., Gao, P., Nazeeruddin, M.K., Grätzel, M., 2013. Sequential deposition as a route to high-performance perovskite-sensitized solar cells. Nature 499, 316–319. http://dx.doi.org/10.1038/nature12340.

Cao, D.H., Stoumpos, C.C., Farha, O.K., Hupp, J.T., Kanatzidis, M.G., 2015. Two-dimensional homologous perovskites as light absorbing materials for solar cell applications. J. Am. Chem. Soc. 137, 7843–7850. http://dx.doi.org/10.1021/jacs.5b03796.

Chin, X.Y., Cortecchia, D., Yin, J., Bruno, A., Soci, C., 2015. Lead Iodide perovskite light-emitting field-effect transistor. Arxiv 6, Adv.

Cohen, R.E., 1992. Origin of ferroelectricity in perovskite oxides. Nature 358, 136–138. http://dx.doi.org/10.1038/358136a0.

Dabhi, S.D., Jha, P.K., 2015. Ab initio study of strained wurtzite InAs nanowires: engineering an indirect–direct band gap transition through size and uniaxial strain. RSC Adv. 5, 89993–90000. http://dx.doi.org/10.1039/C5RA16512A.

Dong, Q., Fang, Y., Shao, Y., Mulligan, P., Qiu, J., Cao, L., Huang, J., Stranks, S.D., Eperon, G.E., Grancini, G., Menelaou, C., Alcocer, M.J., Leijtens, T., Herz, L.M., Petrozza, A., Snaith, H.J., Lee, M.M., Teuscher, J., Miyasaka, T., Murakami, T.N.,

Snaith, H.J., Mei, A., Li, X., Liu, L., Ku, Z., Liu, T., Rong, Y., Xu, M., Hu, M., Chen, J., Yang, Y., Grätzel, M., Han, H., Xing, G., Mathews, N., Lim, S.S., Yantara, N., Liu, X., Sabba, D., Grätzel, M., Mhaisalkar, S., Sum, T.C., Tan, Z.K., Moghaddam, R.S., Lai, M.L., Docampo, P., Higler, R., Deschler, F., Price, M., Sadhanala, A., Pazos, L.M., Credgington, D., Hanusch, F., Bein, T., Snaith, H.J., Friend, R.H., Dong, R., Kim, J., Lee, S.H., Lee, J.H., Hong, K.H., Noel, N.K., Abate, A., Stranks, S.D., Parrott, E.S., Burlakov, V.M., Goriely, A., Snaith, H.J., Shkrob, I.A., Marin, T.W., Xiao, Z., Dong, Q., Bi, C., Shao, Y., Yuan, Y., Huang, J., Baikie, T., Fang, Y., Kadro, J.M., Schreyer, M., Wei, F., Mhaisalkar, S.G., Graetzel, M., White, T.J., Manser, J.S., Kamat, P.V., Stranks, S.D., Burlakov, V.M., Leijtens, T., Ball, J.M., Goriely, A., Snaith, H.J., Bube, R.H., Stoumpos, C.C., Malliakas, C.D., Kanatzidis, M.G., Wehrenfennig, C., Eperon, G.E., Johnston, M.B., Snaith, H.J., Herz, L.M., Poglitsch, A., Weber, D., Leever, B.J., Bailey, C.A., Marks, T.J., Hersam, M.C., Durstock, M.F., Mora-Seró, I., Garcia-Belmonte, G., Boix, P.P., Vázquez, M.A., Bisquert, J., Devanathan, R., Corrales, L.R., Gao, F., Weber, W.J., 2015. Solar cells. Electron-hole diffusion lengths > 175 μm in solution-grown CH3NH3PbI3 single crystals. Science 347, 967–970. http://dx.doi.org/10.1126/science.aaa5760.

Egger, D.A., Kronik, L., 2014. Role of dispersive interactions in determining structural properties of organic-inorganic halide perovskites: Insights from first-principles calculations. J. Phys. Chem. Lett. 5, 2728–2733. http://dx.doi.org/10.1021/jz5012934.

El alamy, A., Bourass, M., Amine, A., Hamidi, M., Bouachrine, M., 2017. New organic dyes based on phenylenevinylene for solar cells: DFT and TD-DFT investigation. Karbala Int. J. Mod. Sci. 3, 75–82.

Eperon, G.E., Stranks, S.D., Menelaou, C., Johnston, M.B., Herz, L.M., Snaith, H.J., 2014. Formamidinium lead trihalide: a broadly tunable perovskite for efficient planar heterojunction solar cells. Energy Environ. Sci. 7, 982. http://dx.doi.org/10.1039/c3ee43822h.

Filip, M.R., Eperon, G.E., Snaith, H.J., Giustino, F., 2014. Steric engineering of metal-halide perovskites with tunable optical band gaps. Nat. Commun. 5. http://dx.doi.org/10.1038/ncomms6757.

Frost, J.M., Walsh, A., 2016. What is moving in hybrid halide perovskite solar cells? Acc. Chem. Res. http://dx.doi.org/10.1021/acs.accounts.5b00431.

Gajdoš, M., Hummer, K., Kresse, G., Furthmüller, J., Bechstedt, F., 2006. Linear optical properties in the projector-augmented wave methodology. Phys. Rev. B – Condens. Matter Mater. Phys. 73.

Gelmetti, I., Cabau, L., Montcada, N.F., Palomares, E., 2017. Selective organic contacts for methyl ammonium lead iodide (MAPI) perovskite solar cells: influence of layer thickness on carriers extraction and carriers lifetime. ACS Appl. Mater. Interfaces 9, 21599–21605. http://dx.doi.org/10.1021/acsami.7b06638.

Giannozzi, P., Baroni, S., Bonini, N., Calandra, M., Car, R., Cavazzoni, C., Ceresoli, D., Chiarotti, G.L., Cococcioni, M., Dabo, I., Dal Corso, A., De Gironcoli, S., Fabris, S., Fratesi, G., Gebauer, R., Gerstmann, U., Gougoussis, C., Kokalj, A., Lazzeri, M., Martin-Samos, L., Marzari, N., Mauri, F., Mazzarello, R., Paolini, S., Pasquarello, A., Paulatto, L., Sbraccia, C., Scandolo, S., Sclauzero, G., Seitsonen, A.P., Smogunov, A., Umari, P., Wentzcovitch, R.M., 2009. QUANTUM ESPRESSO: a modular and open-source software project for quantum simulations of materials. J. Phys. Condens. Matter 21, 395502–395521. http://dx.doi.org/10.1088/0953-8984/21/39/395502.

Green, M.A., Ho-Baillie, A., Snaith, H.J., 2014. The emergence of perovskite solar cells. Nat. Photon. http://dx.doi.org/10.1038/nphoton.2014.134.

Harl, J., Kresse, G., Sun, L.D., Hohage, M., Zeppenfeld, P., 2007. Ab initio reflectance difference spectra of the bare and adsorbate covered Cu(110) surfaces. Phys. Rev. B – Condens. Matter Mater. Phys. 76.

He, M., Chen, Y., Liu, H., Wang, J., Fang, X., Liang, Z., 2015. Chemical decoration of $CH_3NH_3PbI_3$ perovskites with graphene oxides for photodetector applications. Chem. Commun. 51, 9659–9661. http://dx.doi.org/10.1039/C5CC02282G.

Heo, J.H., Im, S.H., Noh, J.H., Mandal, T.N., Lim, C.S., Chang, J.A., Lee, Y.H., Kim, H.J., Sarkar, A., Nazeeruddin, M.K., Grätzel, M., Seok, S. Il, 2013. Efficient inorganic-organic hybrid heterojunction solar cells containing perovskite compound and polymeric hole conductors. Nat. Photonics 7, 486–491. http://dx.doi.org/10.1038/nphoton.2013.80.

Ishihara, T., Takahashi, J., Goto, T., 1989. Exciton state in two-dimensional perovskite semiconductor $(C_{10}H_{21}NH_3)_2PbI_4$. Solid State Commun. 69, 933–936. http://dx.doi.org/10.1016/0038-1098(89)90935-6.

Jeng, J.Y., Chiang, Y.F., Lee, M.H., Peng, S.R., Guo, T.F., Chen, P., Wen, T.C., 2013. $CH_3NH_3PbI_3$ perovskite/fullerene planar-heterojunction hybrid solar cells. Adv. Mater. 25, 3727–3732. http://dx.doi.org/10.1002/adma.201301327.

Jeon, N.J., Noh, J.H., Kim, Y.C., Yang, W.S., Ryu, S., Seok, S. Il, 2014. Solvent engineering for high-performance inorganic-organic hybrid perovskite solar cells. Nat. Mater. 13, 897–903. http://dx.doi.org/10.1038/nmat4014.

Jung, H.S., Park, N.G., 2015. Perovskite solar cells: from materials to devices. Small. http://dx.doi.org/10.1002/smll.201402767.

Kamminga, M.E., Fang, H.H., Filip, M.R., Giustino, F., Baas, J., Blake, G.R., Loi, M.A., Palstra, T.T.M., 2016. Confinement effects in low-dimensional lead iodide perovskite hybrids. Chem. Mater. 28, 4554–4562. http://dx.doi.org/10.1021/acs.chemmater.6b00809.

Kim, H.S., Lee, C.R., Im, J.H., Lee, K.B., Moehl, T., Marchioro, A., Moon, S.J., Humphry-Baker, R., Yum, J.H., Moser, J.E., Grätzel, M., Park, N.G., 2012. Lead iodide perovskite sensitized all-solid-state submicron thin film mesoscopic solar cell with efficiency exceeding 9%. Sci. Rep. 2. http://dx.doi.org/10.1038/srep00591.

Kojima, A., Teshima, K., Shirai, Y., Miyasaka, T., 2009. Organometal halide perovskites as visible-light sensitizers for photovoltaic cells. J. Am. Chem. Soc. 131, 6050–6051. http://dx.doi.org/10.1021/ja809598r.

Lee, M.M., Teuscher, J., Miyasaka, T., Murakami, T.N., Snaith, H.J., 2012. Efficient hybrid solar cells based on meso-superstructured organometal halide perovskites. Science (80-.) 338, 643–647.

Lee, Y., Kwon, J., Hwang, E., Ra, C.H., Yoo, W.J., Ahn, J.H., Park, J.H., Cho, J.H., 2015. High-performance perovskite-graphene hybrid photodetector. Adv. Mater. 27, 41–46. http://dx.doi.org/10.1002/adma.201402271.

Leilaeioun, M., Holman, Z.C., 2016. Accuracy of expressions for the fill factor of a solar cell in terms of open-circuit voltage and ideality factor. J. Appl. Phys. 120. http://dx.doi.org/10.1063/1.4962511.

Li, Z., Kulkarni, S.A., Boix, P.P., Shi, E.Z., Cao, A.Y., Fu, K.W., Batabyal, S.K., Zhang, J., Xiong, Q.H., Wong, L.H., Mathews, N., Mhaisalkar, S.G., 2014. laminated carbon nanotube networks for metal electrode-free efficient perovskite solar cells. ACS Nano 8, 6797–6804. http://dx.doi.org/10.1021/nn501096h.

Liu, J., Xue, Y., Wang, Z., Xu, Z.Q., Zheng, C., Weber, B., Song, J., Wang, Y., Lu, Y., Zhang, Y., Bao, Q., 2016. Two-dimensional $CH_3NH_3PbI_3$ perovskite: synthesis and optoelectronic application. ACS Nano 10, 3536–3542. http://dx.doi.org/10.1021/acsnano.5b07791.

Liu, M., Johnston, M.B., Snaith, H.J., 2013. Efficient planar heterojunction perovskite solar cells by vapour deposition. Nature 501, 395–398. http://dx.doi.org/10.1038/nature12509.

Logan, P., Peng, X., 2009. Strain-modulated electronic properties of Ge nanowires: a first-principles study. Phys. Rev. B – Condens. Matter Mater. Phys. 80.

Mitzi, D.B., 2004. Solution-processed inorganic semiconductors. J. Mater. Chem. 14, 2355. http://dx.doi.org/10.1039/b403482a.

Mitzi, D.B., 2001. Templating and structural engineering in organic–inorganic perovskites. J. Chem. Soc. Dalt. Trans. 1–12. http://dx.doi.org/10.1039/b007070j.

Mitzi, D.B., Feild, C.A., Harrison, W.T.A., Guloy, A.M., 1994. Conducting tin halides with a layered organic-based perovskite structure. Nature 369, 467–469. http://dx.doi.org/10.1038/369467a0.

Natl. Renew. Energy Lab. N.R.E.L. URL < https://www.nrel.gov/pv/assets/images/efficiency-chart.png >.

Noh, J.H., Im, S.H., Heo, J.H., Mandal, T.N., Seok, S. Il, 2013. Chemical management for colorful, efficient, and stable inorganic-organic hybrid nanostructured solar cells. Nano Lett. 13, 1764–1769. http://dx.doi.org/10.1021/nl400349b.

Peña, M.A., Fierro, J.L.G., 2001. Chemical structures and performance of perovskite oxides. Chem. Rev. http://dx.doi.org/10.1021/cr980129f.

Perdew, J.P., Burke, K., 1996. Generalized gradient approximation for the exchange-correlation hole of a many-electron system. Phys. Rev. B – Condens. Matter Mater. Phys. 54, 16533–16539. http://dx.doi.org/10.1103/PhysRevB.54.16533.

Pillai, S.B., Narayan, S., Dabhi, S.D., Jha, P.K., 2016. First principles calculation of two dimensional antimony and antimony arsenide. In: AIP Conference Proceedings. < https://doi.org/10.1063/1.4947988 >.

Quarti, C., Mosconi, E., Ball, J.M., D'Innocenzo, V., Tao, C., Pathak, C., Petrozza, A., Snaith, H., De Angelis, F., Pathak, S., Petrozza, A., Snaith, H., De Angelis, F., 2015. Structural and optical properties of methylammonium lead iodide across the tetragonal to cubic phase transition: implications for perovskite solar cells. Energy Environ. Sci. 16, 155–163. http://dx.doi.org/10.1039/C5EE02925B.

Ryu, S., Noh, J.H., Jeon, N.J., Kim, Y.C., Yang, W.S., Seo, J., Seok, S. Il, 2014. Voltage output of efficient perovskite solar cells with high open-circuit voltage and fill factor. Energy Environ. Sci. 7, 2614–2618. http://dx.doi.org/10.1039/C4EE00762J.

Sha, W.E.I., Ren, X., Chen, L., Choy, W.C.H., Sha, W.E.I., Ren, X., Chen, L., Choy, W.C.H., 2015. The efficiency limit of CH3NH3PbI3 perovskite solar cells. The efficiency limit of CH 3 NH 3 PbI 3 perovskite solar cells 221104. < https://doi.org/10.1063/1.4922150 >.

Shao, Y., Xiao, Z., Bi, C., Yuan, Y., Huang, J., 2014. Origin and elimination of photocurrent hysteresis by fullerene passivation in $CH_3NH_3PbI_3$ planar heterojunction solar cells. Nat. Commun. 5. http://dx.doi.org/10.1038/ncomms6784.

Snaith, H.J., 2013. Perovskites: the emergence of a new era for low-cost, high-efficiency solar cells. J. Phys. Chem. Lett. 4, 3623–3630. http://dx.doi.org/10.1021/jz4020162.

Song, J., Xu, L., Li, J., Xue, J., Dong, Y., Li, X., Zeng, H., 2016. Monolayer and few-layer all-inorganic perovskites as a new family of two-dimensional semiconductors for printable optoelectronic devices. Adv. Mater. 4861–4869. http://dx.doi.org/10.1002/adma.201600225.

Spina, M., Lehmann, M., Náfrádi, B., Bernard, L., Bonvin, E., Gaál, R., Magrez, A., Forrõ, L., Horváth, E., 2015. Microengineered $CH_3NH_3PbI_3$ nanowire/graphene phototransistor for low-intensity light detection at room temperature. Small 11, 4824–4828. http://dx.doi.org/10.1002/smll.201501257.

Spina, M., Nafradi, B., Tohati, H.M., Kamaras, K., Bonvin, E., Gaal, R., Forro, L., Horvath, E., 2016. Ultrasensitive 1D field-effect phototransistors: $CH_3NH_3PbI_3$ nanowire sensitized individual carbon nanotubes. Nanoscale 8, 4888–4893. http://dx.doi.org/10.1039/c5nr06727h.

Stoumpos, C.C., Malliakas, C.D., Kanatzidis, M.G., 2013. Semiconducting tin and lead iodide perovskites with organic cations: Phase transitions, high mobilities, and near-infrared photoluminescent properties. Inorg. Chem. 52, 9019–9038. http://dx.doi.org/10.1021/ic401215x.

Stranks, S.D., Eperon, G.E., Grancini, G., Menelaou, C., Alcocer, M.J.P., Leijtens, T., Herz, L.M., Petrozza, A., Snaith, H.J., 2013. Electron-hole diffusion lengths exceeding 1 micrometer in an organometal trihalide perovskite absorber. Science (80-.) 342, 341–344.

Tan, Z.-K., Moghaddam, R.S., Lai, M.L., Docampo, P., Higler, R., Deschler, F., Price, M., Sadhanala, A., Pazos, L.M., Credgington, D., Hanusch, F., Bein, T., Snaith, H.J., Friend, R.H., 2014. SI: Bright light-emitting diodes based on organometal halide perovskite. Nat. Nanotechnol. 9, 1–6. http://dx.doi.org/10.1038/nnano.2014.149.

Wang, Y., Zhang, Y., Lu, Y., Xu, W., Mu, H., Chen, C., Qiao, H., Song, J., Li, S., Sun, B., Cheng, Y.B., Bao, Q., 2015. Hybrid graphene-perovskite phototransistors with ultrahigh responsivity and gain. Adv. Opt. Mater. 3, 1389–1396. http://dx.doi.org/10.1002/adom.201500150.

Wang, Z., Liu, J., Xu, Z.-Q., Xue, Y., Jiang, L., Song, J., Huang, F., Wang, Y., Zhong, Y.L., Zhang, Y., Cheng, Y.-B., Bao, Q., 2016. Wavelength-tunable waveguides based on polycrystalline organic–inorganic perovskite microwires. Nanoscale 8, 6258–6264.

http://dx.doi.org/10.1039/C5NR06262D.
Weber, D., 1978. CH3NH3PbX3, ein Pb (II)-system mit kubischer perowskitstruktur/CH3NH3PbX3, a Pb (II)-system with cubic perovskite structure. Z. Naturforsch. B 33, 1443–1445.
Whalley, L.D., Frost, J.M., Jung, Y.-K., Walsh, A., 2017. Perspective: theory and simulation of hybrid halide perovskites. J. Chem. Phys. 146, 220901. http://dx.doi.org/10.1063/1.4984964.
Yang, J., Siempelkamp, B.D., Liu, D., Kelly, T.L., 2015. An Investigation of CH3NH3PbI3 degradation rates and mechanisms in controlled humidity environments using in situ techniques. ACS Nano Adv. http://dx.doi.org/10.1021/nn506864k.
Yin, W.-J., Shi, T., Yan, Y., 2014a. Unusual defect physics in $CH_3NH_3PbI_3$ perovskite solar cell absorber. Appl. Phys. Lett. 104, 063903/1–063903/4.
Yin, W.J., Shi, T., Yan, Y., 2014b. Unique properties of halide perovskites as possible origins of the superior solar cell performance. Adv. Mater. 26, 4653–4658. http://dx.doi.org/10.1002/adma.201306281.
Yin, W.W., Yang, J.J., Kang, J., Yan, Y., Wei, S., 2015. Halide perovskite materials for solar cells: a theoretical review. J. Mater. Chem. A 3, Adv. 8926–8942. http://dx.doi.org/10.1039/C4TA05033A.
You, P., Liu, Z., Tai, Q., Liu, S., Yan, F., 2015. Efficient semitransparent perovskite solar cells with graphene electrodes. Adv. Mater. 27, 3632–3638. http://dx.doi.org/10.1002/adma.201501145.
Yu, L., Zunger, A., 2012. Identification of potential photovoltaic absorbers based on first-principles spectroscopic screening of materials. Phys. Rev. Lett. 108, 1–5. http://dx.doi.org/10.1103/PhysRevLett. 108.068701.
Zhang, Y.-Y., Chen, S., Xu, P., Xiang, H., Gong, X.-G., Walsh, A., Wei, S., 2015. Intrinsic instability of the hybrid halide perovskite semiconductor $CH_3NH_3PbI_3$. Nat. Commun. 11. http://dx.doi.org/10.1021/acs.jpclett.5b01666.
Zhou, H., Chen, Q., Li, G., Luo, S., Song, T.-b., Duan, H.-S., Hong, Z., You, J., Liu, Y., Yang, Y., 2014. Interface engineering of highly efficient perovskite solar cells. Science (80-.) 345, 542–546.
Zhou, Q., Jiao, D., Fu, K., Wu, X., Chen, Y., Lu, J., Yang, S., 2016. Two-dimensional device modeling of $CH_3NH_3PbI_3$ based planar heterojunction perovskite solar cells. Sol. Energy 123, 51–56. http://dx.doi.org/10.1016/j.solener.2015.11.009.
Zhu, H., Fu, Y., Meng, F., Wu, X., Gong, Z., Ding, Q., Gustafsson, M.V., Trinh, M.T., Jin, S., Zhu, X.Y., 2015. Lead halide perovskite nanowire lasers with low lasing thresholds and high quality factors. Nat. Mater. 14, 636–642. http://dx.doi.org/10.1038/nmat4271.